



## City Research Online

### City, University of London Institutional Repository

---

**Citation:** Yang, Y., Zhang, Y. & Fu, F. (2022). Performance and design of RAC-filled steel RHS beams. *Journal of Building Engineering*, 46, 103734. doi: 10.1016/j.jobe.2021.103734

This is the accepted version of the paper.

This version of the publication may differ from the final published version.

---

**Permanent repository link:** <https://openaccess.city.ac.uk/id/eprint/27132/>

**Link to published version:** <https://doi.org/10.1016/j.jobe.2021.103734>

**Copyright:** City Research Online aims to make research outputs of City, University of London available to a wider audience. Copyright and Moral Rights remain with the author(s) and/or copyright holders. URLs from City Research Online may be freely distributed and linked to.

**Reuse:** Copies of full items can be used for personal research or study, educational, or not-for-profit purposes without prior permission or charge. Provided that the authors, title and full bibliographic details are credited, a hyperlink and/or URL is given for the original metadata page and the content is not changed in any way.

# Performance and design of RAC-filled steel RHS beams

You-Fu Yang<sup>a,\*</sup>, Yu-Qin Zhang<sup>a</sup>, Feng Fu<sup>b</sup>

<sup>a</sup> State Key Laboratory of Coastal and Offshore Engineering, Dalian University of Technology, Dalian 116024, China

<sup>b</sup> Department of Civil Engineering, School of Mathematics, Computer Science & Engineering, City University of London, Northampton Square, London, UK

**Abstract:** Research on steel hollow sections filled with recycled aggregate concrete (RAC) has been recently gained attention across the world. This is because the RAC-filled steel hollow section reuse the waste concrete, while, still achieving good structural performance. This paper studies the static performance of RAC-filled steel rectangular hollow section (RHS) beams. Ten beams with various recycled coarse aggregate (RCA) replacement ratio ( $r$ ), depth-to-width ratio ( $\beta$ ) and width-to-thickness ratio ( $B/t$ ) were tested. The results show that, after the mid-span deflection exceeds 6 percentage of effective span, the top flange of the tube and part of the adjacent side walls of the tube buckled in the pure bending zone for all tests, whilst cracking was observed at the bottom flange of the tube within pure bending zone of some beams. Accordingly, for the concrete core, both crushing at the tube buckling position and cracks extended towards the compression zone are observed. The moment-deflection (strain) relationship of the specimens can be divided into three key stages, namely, elastic, elastic-plastic and hardening. In general, moment capacity and flexural stiffness of the specimens reduce with the augment of  $B/t$  and the decrease of  $\beta$  under the same width. A finite element (FE) model that can efficiently reproduce the failure process and moment-deformation curves of RAC-filled steel RHS beams is also developed, and the FE is further used to discover the influence of  $r$  and  $\beta$  on working mechanism of such composite beams. Finally, based on the parametric analysis, the design equations for moment capacity of RAC-filled steel RHS beams are developed, and the accuracy of the simplified equations is verified by the experimental results. Meanwhile, the test results also proved that the approach in ACI 318 code is the more suitable method for the flexural stiffness prediction of RAC-filled steel RHS beams.

**Keywords:** RAC-filled steel RHS beam; Experimental behaviour; Finite element (FE) model; Mechanical indexes; Simplified equations.

\*Corresponding author. Tel.: 86-411-8470 8510; Fax: 86-411-8467 4141.

*E-mail address:* youfuyang@163.com (Dr. You-Fu Yang).

# 1. Introduction

1 The use of recycled aggregate concrete (RAC) can solve the problems of environmental pollution by  
2 reuse of construction wastes, therefore tackle the issue of shortage of natural aggregates [1, 2]. At  
3 present, RAC technology has become one of the significant focuses in engineering and scientific  
4 research [3]. Existing studies indicate that, due to more cement mortar attached to the surface, the  
5 recycled aggregates have higher porosity, water absorption and crushing index, and lower density  
6 compared to the natural aggregates. As a result, the strength and modulus of elasticity of RAC are  
7 generally lower, and simultaneously the shrinkage and creep are larger than the normal concrete (NC)  
8 with the same mix proportion [1]. In view of the above inevitable disadvantages, RAC is mainly used  
9 as non-structural components, and seldom used as structural members [4]. This seriously impedes the  
10 process of using RAC in practical engineering structures.

11 Over the last twenty years, steel hollow sections filled with RAC have gained more attention as  
12 the constraint to the RAC from outer tube makes the disadvantage of RAC to be improved [5-7], and  
13 the presence of RAC can also delay or avoid local buckling of thin-walled steel tube, which is  
14 consistent with the role of core concrete in conventional concrete-filled steel tube (CFST) [8]. For the  
15 sake of clarifying the performance of RAC-filled steel tube and further obtaining the corresponding  
16 design approaches, researchers have carried out a large number of exploration and innovation, as  
17 reviewed in Yang et al. [9, 10]. The findings show that, the property of the core RAC and the bond  
18 between the core RAC and the outer steel tube dominate the responses of the RAC-filled steel tube  
19 under various loads. Nevertheless, most previous studies focused on RAC-filled circular steel tubes  
20 [7, 9, 10].

21 Similar to conventional CFST, RAC-filled steel rectangular hollow section (RHS) has the  
22 advantages of larger moment of inertia about major axis [8, 11], and at the same time the rectangular  
23 cross-section is more convenient for welding and anchoring. Moreover, the beam-column joints of  
24 RAC-filled steel RHS structures are usually simpler than those of RAC-filled steel circular hollow  
25 section (CHS) structures. The study on flexural performance of RAC-filled rectangular (including  
26  
27  
28  
29  
30  
31  
32  
33  
34  
35  
36  
37  
38  
39  
40  
41  
42  
43  
44  
45  
46  
47  
48  
49  
50  
51  
52  
53  
54  
55  
56  
57  
58  
59  
60  
61  
62  
63  
64  
65

square) steel hollow sections, such as the flexural stiffness and moment capacity, is the basis for understanding the behaviour of this new type of member under the combination of flexure and compression/tension. However, little research has been done so far. Table 1 chronologically presents a summary of the existing experiments on concrete-filled rectangular (including square) steel tube beams, in which  $D$ ,  $B$  and  $t$  are the depth, width and wall thickness of steel RHS respectively,  $\beta(=D/B)$  is the depth-to-width ratio, and  $r$  is the recycled coarse aggregate (RCA) replacement ratio, which equals to the mass ratio of RCA to total coarse aggregate. It is shown that, the objects of most tests are NC-filled carbon steel tube beams, and only a small amount of RAC-filled square carbon/stainless steel tube beams with recycled aggregate replacement ratio up to 75% have been reported by our research group [19, 21]. Currently, no theoretical analysis on the structural performance of RAC-filled rectangular (including square) steel tube beams was reported in the literature. Therefore, further tests and theoretical modelling of RAC-filled steel RHS beams with recycled aggregate replacement ratio up to 100% are necessary.

The aim of the present research is to further investigate the static performance of RAC-filled steel RHS beams and provide the simplified equations for designers. Four-point bending tests were performed on ten RAC-filled steel RHS beams to evaluate their flexural behaviour. The influence of different ratios of depth-to-width, RCA replacement and width-to-thickness were investigated in these tests. In addition, the behaviour of RAC-filled steel RHS beams was further simulated using a finite element (FE) model, and the effect of various parameters on the working mechanism of this new type of composite beams was then analyzed. Finally, the simplified equations for the moment capacity of RAC-filled steel RHS beams were developed. Furthermore, the existing approaches for the flexural stiffness of RAC-filled steel RHS in design codes were also evaluated.

## **2. Experimental program**

### ***2.1. Design and fabrication of the specimens***

Four-point bending tests on ten RAC-filled steel RHS beam specimens were conducted, and the main parameters included: 1) depth-to-width ratio ( $\beta$ ), from 1.0 to 2.0; 2) recycled coarse aggregate (RCA)

replacement ratio ( $r$ ), from 0 (i.e. NC) to 100%; and width-to-thickness ratio ( $B/t$ ), 31.1 and 60.9.

All specimens had the same length and width, which were 1200 mm and 120 mm, respectively, and thus the variation of  $\beta$  can also be regarded as that of shear span-to-depth ratio ( $s/D$ ) under the same shear span ( $s$ ). Fig. 1 shows the cross-section of the specimens. The details of the specimens are summarized in Table 2, where  $f_y$  is the yield strength of steel,  $f_{cu}$  is the cubic compressive strength of concrete while conducting beam tests,  $M_{u,e}$  is the experimental moment capacity, and  $K_e$  is the experimental flexural stiffness. The labels in Table 2 represent the experimental parameters of each specimen, and parts 1, 2 and 3 represent  $B/t$ ,  $r$  and  $\beta$ , respectively, in which ‘L’ and ‘S’ in part 1 denote  $B/t$  of 60.9 and 31.1, respectively.

The steel RHS of all specimens consists of two identical U-shaped profiles welding together by two straight welds (see Fig. 1), and each U-shaped profile was made of a steel plate of the same length as the specimen through cold forming (bending). Before casting concrete, a rectangular steel plate was welded to one end of steel RHS. Concrete was poured vertically into the unsealed end of steel RHS. The specimens were placed vertically for concrete curing, and the other endplate was welded to the unsealed end of steel RHS after the concrete core was cured for 14 days. In addition, to clearly show the destruction process and failure pattern of the specimens, white grid lines were drawn on the outer surface of each steel RHS.

## 2.2. Material properties

The properties of steel were acquired based on tensile tests of three strips, and the average values are summarized in Table 3, where  $f_u$  is the tensile strength,  $E_s$  is the modulus of elasticity,  $\varepsilon_y$  is the yield strain,  $\mu_s$  is the Poisson’s ratio, and  $e_f$  is the fracture elongation.

Two types of RAC with  $r$  of 50% and 100% respectively, together with one type of NC (for comparison), were produced, and the mix proportions of concrete are presented in Table 4. The water-to-cement ratio of concrete was 0.45, and simultaneously the polycarboxylate water reducing agent of 0.6% cement mass was blended to ensure the workability of fresh mixtures. The destructed concrete blocks were used to obtain RCA in two types of RAC, and calcareous stone was selected as

1 the natural coarse aggregate (NCA). Two types of coarse aggregate had similar cumulative percent  
2 passing sieve. The detailed physical properties of RCA and NCA were described in Yang et al. [27].  
3 Other materials used in the production of concrete included: Portland cement (P.O 42.5), natural  
4 medium sand and running water.  
5  
6

7  
8 When producing each type of concrete, 6 cubes with side length of 150 mm were tested to  
9 determine the compressive strength, whilst 3 prisms with dimensions of 150 mm×150 mm×300 mm  
10 were tested to determine the modulus of elasticity ( $E_c$ ). The slump test was also carried out to measure  
11 the slump of concrete ( $S_c$ ). The properties of concrete based on the average of three test results are  
12 also given in Table 4, where  $f_{cu,28}$  are the cubic compressive strength at 28 days. The results in Table  
13 4 indicate that,  $f_{cu}$ ,  $E_c$  and  $S_c$  of RAC are 1.3%~2.6%, 9.6%~17.6% and 21.1%~42.1% lower than  
14 the corresponding NC, and the higher the RCA replacement ratio ( $r$ ), the worse are the properties.  
15 There are similar findings in the previous experiments [3, 7, 19, 21].  
16  
17

### 18 **2.3. Test set-up and instrumentation**

19  
20 A commonly used four-point bending test rig was designed, as demonstrated in Fig. 2. There was no  
21 device to restrict the lateral deformation as the specimens have a rectangular cross-section. A fixed  
22 hinge support and a rolling hinge support were placed between the bottom of beam specimen and the  
23 top of two reaction blocks, and their spacing equaled to the effective span ( $L_e$ ), i.e. 1000 mm.  
24  
25 Meanwhile, the other two supports with the spacing of  $L_e/2$  corresponding to two quartiles were  
26 arranged between the top of beam specimen and the bottom of a rigid girder to form the pure bending  
27 zone. The concentrated vertical loads ( $P$ ) acting on the mid-span were applied by a 5000 kN tester  
28 and a load cell was used to record the loading history. Therefore, the moment ( $M$ ) in the pure bending  
29 zone of the specimen was equal to  $P \cdot L_e/8$  based on the test rig in this study.  
30  
31

32  
33 For each specimen, there were 5 displacement transducers, among which two placed on the top of  
34 specimen to measure the displacements of the supports and three on the bottom of specimen were  
35 used for recording the deflections of the quartiles. Moreover, to monitor the strain development, a  
36 total of 18 strain gauges (12 longitudinal and 6 transverse) were pasted in the mid-span section of the  
37  
38  
39  
40  
41  
42  
43  
44  
45  
46  
47  
48  
49  
50  
51  
52  
53  
54  
55  
56  
57  
58  
59  
60  
61  
62  
63  
64  
65

outer tube of each specimen, and the detailed location of strain gauges is also demonstrated in Fig. 2.

The load control approach was used when the applied load was less than 80% of the estimated capacity [6], and the loading rate was 0.5 kN/s. After the applied load reached 80% of the estimated capacity, the displacement control approach was adopted and the rate of deflection at the mid-span was equal to 1.0 mm/min. The specimens were continually loaded until the steel RHS had major cracks or the mid-span deflection was greater than 8% of the effective span.

#### **2.4. Test results and discussion**

Generally, all specimens showed good load-bearing capacity and deformability. At the beginning of the test, the moment of the specimen increased almost linearly with the increase of deformation, and the specimen had no visible damage. As the materials entered elastic-plastic stage and the neutral axis raised, the growth of deformation was gradually faster than that of moment, and there were several local buckling observed at the top flange of the tube within the pure bending zone and the sound of concrete crushing. After reaching certain deformation, the rate of deformation increase was much higher than that of moment, and the local buckling on the top flange of the tube became more significant, which further led to local buckling in part of the side walls. Moreover, in the later loading stage of some specimens, tensile cracking of the bottom flange of the tube occurred, which resulted in the drop of moment.

Fig. 3 shows the final failure pattern of the specimens under different parameters. It can be observed that, all specimens exhibit routine deflection shape [19, 21], and there are 2-4 local buckling observed on top flange of the tube (point out by arrows) as well as part of side walls adjacent to it within the pure bending zone. In addition, tensile crack of steel RHS (point out by triangle) is also noticed in some specimens. Based on a detailed observation on the phenomenon in Fig. 3, it can be concluded that, there are three representative failure patterns of steel RHS, as shown in Fig. 4. For specimens with  $r = 50\%$  and  $\beta = 1.0(1.5)$  [i.e. L(S)-50%-1.0(1.5)], there are only several local buckling on top flange and part of side walls of the tube (see Fig. 4(a)), and no cracking on bottom flange of the tube occurs, which is analogous to the previous findings in the experiments of RAC-filled steel RHS

1 beam specimens with  $\beta = 1.0$  [19, 21]. For specimens L(S)-0-1.5, S-100%-1.5 and S-50%-2.0, in  
2 addition to several local buckling on top flange and part of side walls of the tube, there is also a slight  
3 tensile crack on bottom flange of the tube (see Fig. 4(b)). For specimens L-100%-1.5 and L-50%-2.0,  
4 besides several local buckling on top flange and part of side walls of the tube, there is also an evident  
5 tensile cracking of the tube throughout part of cross-section, as indicated in Figs. 3(a) and (c) and Fig.  
6 4(c). This can be explained that, compared with specimens with  $\beta = 1.0$ , the distance from bottom  
7 flange of the tube to the centroid axis increased with the increase of  $\beta$  and the bottom flange of the  
8 tube suffered a quicker raise in the tensile strain, and therefore more prone to cracking. Moreover, the  
9 difference in buckling position and crack pattern is mainly due to the random distribution of material  
10 defects. It can also be found from Fig. 3 that, generally, the local buckling on top flange of the tube  
11 is the greatest at the location where tensile crack of bottom flange of the tube is observed, considering  
12 that the increase in curvature of the cracked section results in a larger compressive strain on top flange  
13 of the tube. Furthermore, regardless of cracking on bottom flange of the tube, the curvature of the  
14 deformed specimens reduces with the increase of  $\beta$  and has no obvious disparity with the variation  
15 of  $r$  and  $B/t$ .

16 After the loading tests, the appearance of concrete core in steel RHS of the specimens includes  
17 crushing at the buckling positions on top flange and part of side walls of the tube, as well as cracking  
18 at the tensile zone below the neutral axis, as demonstrated in Fig. 5. Generally, with the decrease of  
19  $\beta$  and  $B/t$ , the average spacing, width and height of tensile cracks reduce. This is due to the fact  
20 that, under the same width ( $B$ ), the outer tube of beams having a lower  $\beta$  and  $B/t$  has a stronger  
21 confinement to its concrete core, which improves the inhibition effect of outer tube on concrete  
22 cracking. In general,  $r$  has no apparent impact on the characteristics of tensile cracks.

23 The recorded moment ( $M$ ) versus mid-span deflection ( $\delta_m$ ) curve of the specimens is plotted in  
24 Fig. 6, where the arrows indicate the beginning of the tensile cracking of steel RHS. It is shown that,  
25 similar to the RAC-filled steel RHS beam specimens with  $\beta = 1.0$  in [19, 21], the  $M - \delta_m$   
26 diagram of RAC-filled steel RHS beams with  $\beta$  up to 2.0 generally includes an initial elastic phase

with large stiffness, an elastic-plastic phase in which the stiffness gradually decreases, and a hardening phase with very small stiffness. In particular, there is a descending stage on the  $M - \delta_m$  curve of the specimens having tensile cracking of outer tube, and the deformability of the specimens with  $\beta = 2.0$  is significantly reduced due to the tensile cracking of outer tube throughout part of cross-section. Generally,  $B/t$  and  $\beta(s/D)$  have a significant effect on the  $M - \delta_m$  curve, whilst  $r$  has a moderate influence.

The relationship between strain ( $\varepsilon$ ) in the mid-span section and moment ( $M$ ) of typical specimens is indicated in Fig. 7, and all other specimens have a similar  $M - \varepsilon$  diagram, where ‘L’ and ‘T’ denote longitudinal and transverse strain, respectively. It can be seen that, the strains at measuring points on top and bottom flange of the tube are the largest, and for longitudinal and transverse strain gauges (a, b, f and g), the Poisson’s effect reverses the signs of them. For top flange of the tube, the strains in the middle (a) are slightly larger than those in the corner (b), as the local buckling gradually recedes from the middle to the corner. However, for bottom flange of the tube, the strains in the middle (g) are generally smaller than those in the corner (f) at the elastic-plastic phase. This is due to the fact that, the corner zone of steel RHS has a stronger interaction between the tube and its concrete core than the flat zone [8], resulting in a slower cracking of concrete core and a faster load transmission. The strain difference of points f and g in the other two phases is small as the concrete does not crack (or slightly crack) and completely crack, respectively. The longitudinal strains at point d are always positive (under tension), indicating that it is below the neutral axis during the whole loading process, as the neutral axis rises due to the invalidation of the cracked concrete. The longitudinal strains of point e are between the longitudinal strains of point d and point f(g) owing to its position. Moreover, for the beams having  $B/t = 60.9$ , the longitudinal strains at point c undergo a variation process from compression to tension and then to compression again; however, for the beams having  $B/t = 31.1$ , the longitudinal strains at point c are kept to be negative (under compression), indicating that it is located above the neutral axis throughout the loading process, as the steel RHS has an improved confinement to its concrete core.

Fig. 8 demonstrates the influence of parameters on  $M - \varepsilon_L$  relationship at points a and g, in which  $\varepsilon_L$  represents the longitudinal strain. It is shown that, under different parameters, the development trend of  $M - \varepsilon_L$  relationship is generally comparable to that of  $M - \delta_m$  curve, and the hardening stage of all  $M - \varepsilon_L$  curves occurs after the steel reaches yield strength. It can also be found that, generally, the  $M - \varepsilon_L$  curves develop steadily after  $\varepsilon_L$  at point g achieving 0.01. As a result, based on the experimental findings of this study and previous research results [18, 19, 21], the moment while the ultimate tensile strain at the midpoint of bottom flange of the tube in the mid-span section equal to 0.01 is defined as the moment capacity ( $M_{u,e}$ ) of RAC-filled steel RHS beams. The  $M_{u,e}$  of the specimens is listed in Table 2.

Fig. 9 shows the relationship between  $\varepsilon_L$  and  $\varepsilon_T$  at the midpoint of both flanges of the tube in the mid-span section, where  $\varepsilon_T$  is the transverse strain. It can be observed that, at the initial loading stage the ratio of  $\varepsilon_T$  to  $\varepsilon_L$  is generally close to  $\mu_s$ , indicating that steel RHS and its concrete core bear the loads respectively; however, after the steel RHS interacts with the concrete core,  $\varepsilon_T/\varepsilon_L$  values become larger than  $\mu_s$  very soon, and with the augment of concrete Poisson's ratio  $\varepsilon_T/\varepsilon_L$  values continually show a trend of improvement. It can also be found that, for the point in the tensile zone (i.e. point g), the experimental parameters have little influence on  $\varepsilon_T/\varepsilon_L$  values. This can be explained that, after concrete cracking only the steel RHS with the same width below the neutral axis is under tension. However, for the point in the compressive zone (i.e. point a),  $\varepsilon_T/\varepsilon_L$  values of the specimens with  $r$  of 50% and 100% are larger than those of the reference beam with  $r = 0$  because of the change in the position of the neutral axis, and  $\varepsilon_T/\varepsilon_L$  values of the specimens generally increase with the growing of  $\beta$  due to the raise of the depth of compression zone. Moreover,  $B/t$  has no consistent effect on the variation in  $\varepsilon_T/\varepsilon_L$  values.

The typical longitudinal strain ( $\varepsilon_L$ ) distribution along the depth ( $D$ ) of the mid-span section is displayed in Fig. 10, where  $y$  is the distance between the measuring point and the centroid,  $m$  ( $=M/M_{u,e}$ ) is the moment level, and  $\varepsilon_L$  is the average longitudinal strain at the symmetric positions. It can be seen that, generally,  $\varepsilon_L$  values are linearly distributed across the depth before reaching  $M_{u,e}$ ;

1 however, after  $M_{u,e}$  is achieved  $\varepsilon_L$  values are no longer linearly distributed across the depth due to  
2 the aggravation of tensile and compression damage of concrete core or the tensile cracking on bottom  
3 flange of the tube. It can also be observed that, the neutral axis continually varies with the increase  
4 of  $m$ .  
5  
6

7  
8 The deflections ( $\delta$ ) along the effective span of two typical specimens are displayed in Fig. 11 by  
9 solid lines, where  $z_l$  is horizontal distance from the measuring point to the fixed hinge support, and  
10 the dashed lines represent the sinusoidal half-waves with the same mid-span deflection as the  
11 measured results. It is shown that, under different  $m$  values, the deflection curves are generally  
12 symmetric about the mid-span section and approximately follow the sinusoidal half-wave. Fig. 11  
13 also shows that, at the later stage of loading, the difference between the measured deflection curves  
14 and the sinusoidal half-waves increases with the increase of  $m$  due to the gradual accumulation of  
15 destruction in materials.  
16  
17

18 For the RAC-filled steel tube or conventional CFST beam specimens under four-point bending,  
19 there are three methods for determining the curvature of the mid-span section. The first method  
20 assumes that the deflections of the specimen accord with the sinusoidal half-wave. The second  
21 method was proposed by Xiong et al. [26], and it assumes that the curvature of each point in the pure  
22 bending zone is the same and the neutral axis position can be obtained by the ‘plane sections remain  
23 plane assumption’. The third method was also suggested by Xiong et al. [26], and it assumes that the  
24 ‘plane sections remain plane after deformation’ and there is no relative slip between steel tube and its  
25 concrete core. The comparison results show that, based on the measured deflections as well as strains  
26 in the mid-span section, the difference in the curvatures obtained by the above three methods is not  
27 obvious, considering that the assumption of ‘deflection conforms to sinusoidal half-wave’ and ‘plane  
28 sections remain plane after deformation’ has been generally confirmed in the tests of this and previous  
29 studies [18, 19]. The curvatures obtained based on the first method are eventually employed in this  
30 paper. Fig. 12 demonstrates the moment ( $M$ ) versus curvature ( $\phi$ ) relationship of the specimens. It is  
31 shown that, the characteristics of  $M - \phi$  curve is similar to that of the corresponding  $M - \delta_m$   
32  
33  
34  
35  
36  
37  
38  
39  
40  
41  
42  
43  
44  
45  
46  
47  
48  
49  
50  
51  
52  
53  
54  
55  
56  
57  
58  
59  
60  
61  
62  
63  
64  
65

curve. Furthermore, the data in Fig. 12 can be used to obtain the flexural stiffness ( $K_e$ ) of the specimens, which is defined as  $0.2M_{ue}/\phi_{0.2}$  [18, 21], where  $\phi_{0.2}$  is the curvature corresponding to  $0.2M_{ue}$ . The  $K_e$  of the specimens is listed in Table 2.

Fig. 13(a) shows the variation in relative position of neutral axis of the specimens with the increase of  $\delta_m$ , where  $x_n$  is the neutral axis height, namely the distance from the neutral axis to the outer edge of bottom flange of the tube, which is obtained based on the longitudinal strain distribution along the cross-sectional depth, as typically shown in Fig. 10. Moreover, the graphic symbols in Fig. 13(a) correspond to  $x_n/D$  when  $M_{u,e}$  is reached. It can be seen that,  $x_n/D$  values of all specimens generally experience the process of first increasing and then decreasing, and  $x_n/D$  values can continue to grow while achieving  $M_{u,e}$ . The raise of neutral axis is caused by the continuous cracking of concrete core in tension, and the neutral axis rises further when  $M_{u,e}$  is reached as the failure of concrete core in compression does not occur yet. After the concrete core is crushed, the longitudinal strain at top flange of the tube develops faster than that at bottom flange of the tube with the aggravation of compressive buckling failure of steel RHS. In addition, the fluctuation of the  $x_n/D - \delta_m$  curves are induced by the material defects and the subtle instability of artificially controlled loading. It can also be observed from Fig. 13(a) that, under the same  $\delta_m$  value,  $x_n/D$  value of the beams having  $B/t$  of 31.1 is smaller than that of the beams having  $B/t$  of 60.9, indicating that the upward movement of neutral axis is inhibited by the reduction of  $B/t$  owing to the improvement in the confinement of steel RHS to its concrete core, that is, slows down the failure process of the specimens. In general,  $\beta$  and  $r$  mainly affect the process of each development stage of the  $x_n/D - \delta_m$  curve and have no consistent influence on the specific  $x_n/D$  value.

The influence of  $B/t$ ,  $\beta$  and  $r$  on the moment capacity ( $M_{u,e}$ ) is exhibited in Fig. 14(a). The outcomes in Fig. 14(a) and Table 2 indicate that,  $B/t$  and  $\beta$  have significant effect on  $M_{u,e}$ , and  $r$  has less effect on  $M_{u,e}$  than the other two factors. Generally,  $M_{u,e}$  rises with the decrease of  $B/t$  and the growing of  $\beta$  owing to the improvement in the confinement of steel RHS to its concrete core and the section modulus about the axis of bending. Under the same condition,  $M_{u,e}$  of the specimens

with  $B/t$  of 31.1 is about 2.23 times that of those with  $B/t = 60.9$ , and  $M_{u,e}$  of the specimens with  $\beta$  of 1.5 and 2.0 is 81.1~105.3% and 173.1~184.8% higher than that of those with  $\beta=1.0$ , respectively. Generally, the difference in  $M_{u,e}$  between the specimens with  $r$  of 50% and 100% and those with  $r = 0$  is from 0 to 5.1%. The difference in the compressive strength of concrete with different  $r$  value is not reflected in the moment capacity, as the cracked concrete core has a very limited contribution to  $M_{u,e}$ .

The variation of the flexural stiffness ( $K_e$ ) with the experimental parameters is displayed in Fig. 14(b). The outcomes in Fig. 14(b) and Table 2 show that, because of the enhanced confinement of steel RHS to its concrete core, modulus of elasticity of concrete as well as cross sectional moment of inertia,  $K_e$  of the beams rises with decreasing  $B/t$  and  $r$  and increasing  $\beta$ . Under the same conditions, the beams having  $B/t$  of 31.1 have 17.6~43.3% higher  $K_e$  values than the relevant beams having  $B/t$  of 60.9.  $K_e$  of the beams with  $r$  of 50% and 100% is 2.5~7.1% and 7.6~15.9% lower than that of those with  $r=0$ , respectively, and  $K_e$  of the beams with  $\beta = 1.5$  and  $\beta = 2.0$  equals to 2.67~2.96 and 5.46~5.75 times that of those with  $\beta = 1.0$ , respectively.

### 3. Finite element (FE) modelling

#### 3.1. Description of the FE model

To numerically investigate the structural performance of RAC-filled steel RHS beams, a non-linear finite element (FE) model was constructed based on ABAQUS software [28].

The elastic properties of steel RHS (i.e.  $E_s$  and  $\mu_s$ ) duplicated those measured by standard tensile tests (see Table 3). Meanwhile, the metal plasticity model was selected to model the plastic properties of steel RHS, which are represented by the relationship between plastic strain and true stress in the software. As previously mentioned, the steel RHSs in present tests were composed of two U-shaped cold-formed profiles, which makes the corner zone have strengthening effect compared with the flat zone, that is, different material properties should be set to the flat and corner zone in the FE modelling.

For the flat zone of steel RHS, the engineering stress ( $\sigma_s$ )-strain ( $\varepsilon_s$ ) relationship proposed in [29] was employed to obtain the true stress versus plastic strain relationship, and the details are as follows:

$$\sigma_s = \begin{cases} E_s \cdot \varepsilon_s & (\varepsilon_s \leq \varepsilon_e) \\ 0.75f_y + 0.5E_s \cdot (\varepsilon_s - \varepsilon_e) & (\varepsilon_e < \varepsilon_s \leq \varepsilon_{e1}) \\ 0.875f_y + 0.1E_s \cdot (\varepsilon_s - \varepsilon_{e1}) & (\varepsilon_{e1} < \varepsilon_s \leq \varepsilon_{e2}) \\ f_y + 0.005E_s \cdot (\varepsilon_s - \varepsilon_{e2}) & (\varepsilon_s > \varepsilon_{e2}) \end{cases} \quad (1)$$

where,  $\varepsilon_e = 0.75 f_y / E_s$ ,  $\varepsilon_{e1} = f_y / E_s$ , and  $\varepsilon_{e2} = 2.25 f_y / E_s$ .

Accordingly, Abdel-Rahman and Sivakumaran [29] also suggested the yield strength for the corner zone of steel RHS, which is related to the ratio of ultimate strength to yield strength in the flat zone and ratio of corner radius to thickness. In this study, the corner radius and the weighted average yield strength of cold-formed steel RHS were obtained based on the proposal in [30] and [31], respectively.

In order to reasonably simplify the calculation and accelerate convergence, the endplates of the beams were treated as an elastic material that has little effect on the structural performance, and in the FE modelling  $1.0 \times 10^8 \text{ N/mm}^2$  and 0.0001 were set to be the modulus of elasticity and Poisson's ratio of the endplates, respectively.

The modulus of elasticity ( $E_c$ ) and Poisson's ratio ( $\mu_c$ ) of concrete core in the tube were obtained according to ACI 318 [32] and FIB [33], respectively. The inelastic property of concrete was simulated using the damaged plasticity model, in which, isotropic damaged elasticity and isotropic tensile/compressive plasticity were included. The equivalent tensile/compressive plastic strain controlled the yielding and failure surface, and the tensile/compressive damage variables were used to characterize softening and stiffness deterioration. The fracture energy cracking criterion in ABAQUS [28] was selected to model the tension stiffening of concrete. Moreover, the engineering stress-strain relationship presented in Yang et al. [9], which has been successfully used to model the static performance of RAC-filled steel RHS stub columns [9] as well as beam-columns [10], was chosen to describe the compressive stress versus inelastic strain relationship, and the detailed formulae are as follows:

$$\sigma_c / \sigma_{c0} = \begin{cases} 2(\varepsilon_c / \varepsilon_{c0}) - (\varepsilon_c / \varepsilon_{c0})^2 & (\varepsilon_c / \varepsilon_{c0} \leq 1) \\ \frac{\varepsilon_c / \varepsilon_{c0}}{a \cdot (\varepsilon_c / \varepsilon_{c0} - 1)^b + \varepsilon_c / \varepsilon_{c0}} & (\varepsilon_c / \varepsilon_{c0} > 1) \end{cases} \quad (2)$$

where,  $\sigma_{c0}$  and  $\varepsilon_{c0}$  are peak stress and the corresponding strain, respectively;  $a = \frac{(f'_c)^{0.1}}{1.2(1+\xi_r)^{0.5}}$ , in

1 which,  $f'_c$  is cylindrical compressive strength of the reference NC and  $\xi_r$  is confinement factor of  
2 composite section [6]; and  $b = 1.6 + 1.5(\varepsilon_c/\varepsilon_{c0})^{-1}$ .

3 The detailed formula of  $\xi_r$  is:  
4

$$5 \quad \xi_r = \alpha \cdot \frac{f_y}{f_{ck,r}} \quad (3)$$

6 where,  $\alpha$  is the steel ratio, which is equal to the area of steel RHS divided by that of concrete core;  
7 and  $f_{ck,r}$  is the characteristic compressive strength of core RAC [36].  
8

9 The steel RHS was modelled by shell elements (S4) using the Simpson's law in thickness direction,  
10 whilst the concrete core and both endplates were simulated by three-dimensional solid elements  
11 (C3D8R). The meshing of the FE model of the beams was realized based on the structured meshing  
12 technology in ABAQUS [28], and the meshing size of  $B/10$  was defined by following the  
13 suggestion of Xiang et al. [34]. In addition, the meshing was refined in the corner zone of steel RHS  
14 to boost the convergence of the FE simulation. Fig. 15 indicates the meshing of the whole FE model  
15 in this study.  
16  
17  
18  
19  
20  
21  
22  
23  
24  
25  
26  
27  
28  
29  
30

31 To replicate the interaction between outer tube and concrete core, the 'hard contact' in the normal  
32 direction and the 'Coulomb friction' model in the tangential directions with the friction coefficient of  
33 0.6 [10] were defined, i.e., the compressive stresses between their interfaces can be transmitted  
34 absolutely and their interfaces can be separated but not interpenetrated. Meanwhile, the shear stresses  
35 can also be transferred along their interfaces, and while the shear stress reaching a critical value the  
36 relative sliding within their interfaces happens [28]. For the interface between endplates and concrete  
37 core, there was only the 'hard contact' in the normal direction, and the tangential interaction was  
38 ignored, seeing that the cross-sectional area is much smaller than the side area along the span direction.  
39 Moreover, the 'shell-to-solid coupling' constraint was applied to duplicate the interface between the  
40 endplates and steel RHS.  
41  
42  
43  
44  
45  
46  
47  
48  
49  
50  
51  
52  
53  
54  
55

56 Fig. 15 demonstrates the boundary conditions of the whole FE model of RAC-filled steel RHS  
57 beams, where the position of the supports and loading points is exactly the same as the tested  
58 specimens. The translational displacements in X, Y and Z directions of one support were constrained  
59  
60  
61  
62  
63  
64  
65

to reproduce the fixed hinge support, whilst the translational displacements in X and Y directions of the other support were constrained to replicate the rolling hinge support. The displacements along Y direction were put on two quartiles of beams until the mid-span deflection exceeded the measured value in the tests.

It is well known that the initial imperfections and residual stresses have significant influence on the behaviour of steel RHSs. However, the research conducted by Tao et al. [35] showed that the effect of the above factors was evidently reduced after filling concrete into the steel RHSs. As a result, the initial imperfections and residual stresses had not been included in the present FE model of RAC-filled steel RHS beams.

### 3.2. Verification of the FE model

Fig. 16 demonstrates the simulated failure patterns of typical specimens in this study, where the steel RHS and the concrete core are described by the Mises stress and the maximum principal strain, respectively. In addition, similar to the experimental appearance,  $r$  has a moderate effect on the simulated failure patterns. The comparison between Fig. 16(a) and Fig. 3 indicates that, in general, the simulated bending deflection of the specimens and several local buckling of steel RHS are consistent with the measured results. It can also be found from the contrast between Fig. 16(b) and Fig. 5 that, the range under tension and the location of maximum principal strain obtained by the FE simulation generally agree well with the measured cracking range and location of cracks of concrete core, respectively. Moreover, the FE simulation results indicate that, the maximum principal strain under tension and compression is mainly concentrated on the pure bending zone, and the relative height of the tension zone in the mid-span section lessens with the decrease of  $B/t$ .

The comparison between the simulated  $M - \delta_m$  curves with the experimental results of this paper and previous studies [19, 21] is shown in Figs. 6 and 17, respectively. The typical comparison between the simulated and measured  $M - \varepsilon_L$  relationship is demonstrated in Fig. 8. Generally, the simulated results have similar development process as the measured ones; however, the initial slope and the stage after reaching  $M_{u,e}$  of the simulated curves are different from those of the measured ones to

1 some extent. This is due to the fact that, the FE model in this study can not yet reproduce the initial  
2 material and geometric defects of the specimens, the deviation of the measuring devices from the  
3 designed positions, as well as the tiny loading eccentricity and friction between the rolling hinge  
4 supports and the contact surfaces in the test apparatus, etc, which are hard to be reasonably quantified  
5 at present. The simulated variation in relative position of neutral axis ( $x_n/D$ ) is plotted in Fig. 13(b),  
6 where the graphic symbols also indicate the  $x_n/D$  value while achieving  $M_{u,e}$ . The comparison  
7 between Fig. 13(b) and Fig. 13(a) indicates that, the simulated variation trend of  $x_n/D$  with  $\delta_m$  and  
8 the value corresponding to  $M_{u,e}$  are generally in consistent with the measured results, and  $B/t$  is  
9 the main factor affecting the variation in  $x_n/D$ , namely,  $x_n/D$  reduces with the decrease of  $B/t$ ,  
10 which can also be observed in Fig. 16(b).  
11  
12  
13  
14  
15  
16  
17  
18  
19  
20  
21  
22

23 The comparison between the simulated ( $M_{u,fe}$ ) and experimental ( $M_{u,e}$ ) moment capacity of RAC-  
24 filled steel RHS beam specimens is presented in Fig. 18, where a total of 18 specimens with  $r$  of  
25 25% to 100% are included. The calculation results indicate that, the mean (minimum=0.893 and  
26 maximum=1.136) and standard deviation (SD) of  $M_{u,fe}/M_{u,e}$  are 1.056 and 0.061, respectively.  
27  
28  
29  
30  
31  
32  
33 Generally, the simulated moment capacities conform well to the experimental results.  
34  
35

36 Based on the above verification, it can be believed that the FE model developed in this paper is  
37 suitable for computing the flexural behaviour of RAC-filled steel RHS, although the simulated results  
38 are different from the measured results to a certain extent.  
39  
40  
41  
42

### 43 **3.3. Analysis of working mechanism**

44  
45 The validated FE model is further used to analyze the effect of  $\beta$  and  $r$  on typical working  
46 mechanism of RAC-filled steel RHS beams under static loading. The basic parameters investigated  
47 in the models covers most of the cases in the initial stage of the using this new type of composite  
48 members in construction engineering practices include:  $\beta = 1.0\sim 2.0$  (keeping the sum of  $D$  and  $B$   
49 as 800 mm),  $L_e = 10D$ ,  $r = 0\sim 100\%$ ,  $f_y=355$  MPa,  $f'_c=50$  MPa, and  $\alpha = 0.1$ .  
50  
51  
52  
53  
54  
55  
56  
57

58 While reaching the moment capacity, the effect of  $\beta$  and  $r$  on longitudinal stress (S33) of  
59 concrete core in the mid-span section is demonstrated in Fig. 19. It is shown that, there are clear  
60  
61  
62  
63  
64  
65

1 tension and compression zone, which are delimited by the neutral axis. Generally, with the increase  
2 of  $\beta$  and  $r$ , the longitudinal stress reduces, considering that a larger  $\beta$  and  $r$  leads to a weaker  
3 overall confinement of steel RHS to its concrete core and a smaller concrete strength, respectively.  
4

5 The influence of  $\beta$  and  $r$  on  $p/f'_c$  at specific positions in the mid-span section is plotted in Fig.  
6 20, where  $p$  is the interaction stress between steel RHS and its concrete core. It can be seen that, at  
7 the initial loading stage, the  $p$  values are very small as the steel RHS and concrete core bear the  
8 loads independently. After the Poisson's ratio of concrete core exceeds that of steel RHS, both  
9 components begin to interact significantly; however, the evolvement of  $p$  in compression zone is  
10 obviously different from that in tension zone, and the  $p$  value in compression zone is generally  
11 greater than that in tension zone under the same  $\delta_m$ . For the compressive corner (point I),  $p$   
12 generally increases with the increase of  $\delta_m$  and there is a slope mutation during the increase of  $p$ .  
13 This may be induced by the start of local buckling on top flange of the tube. For the tensile corner  
14 (point J), the  $p - \delta_m$  curve is divided into two phases by the yielding of bottom flange of the tube,  
15 and in the first phase the  $p - \delta_m$  curve at point J is similar to that at point I, whilst in the second  
16 phase  $p$  decreases slightly or first decreases slightly and then increase as  $\delta_m$  increases. This may  
17 be induced by the extension of the yielding of side walls of the tube and cracking of concrete core  
18 with the increase of  $\delta_m$ . Generally,  $p$  increases with the reduction of  $\beta$  and the increment of  $r$   
19 due to the improvement in the confinement of steel RHS to its concrete core.  
20  
21  
22  
23  
24  
25  
26  
27  
28  
29  
30  
31  
32  
33  
34  
35  
36  
37  
38  
39  
40  
41  
42

#### 43 **4. Simplified formulae**

44 It is clear that, for the RAC-filled cold-formed steel RHS beams, the calculation of moment capacity  
45 and flexural stiffness becomes quite complicated due to the geometric complications of the rounded  
46 corners, and the difference in material properties between corner and flat zone need to be further  
47 considered for calculating the moment capacity. In view of this, the simulated flexural behaviour of  
48 RAC-filled cold-formed steel RHS beams and RAC-filled welded steel RHS beams with right corners  
49 based on the verified FE model is compared, in which both steel RHSs have the same geometry  
50 parameters (i.e.  $D$ ,  $B$  and  $t$ ) and the yield strength (flat zone of cold-formed one), and the results  
51  
52  
53  
54  
55  
56  
57  
58  
59  
60  
61  
62  
63  
64  
65

under different parameters are displayed in Fig. 21. It is shown that, with the variation of critical parameters, the RAC-filled steel RHS beams with different outer tube generally have the similar  $M - \varepsilon_L$  curve under the same parameters, and the overall difference in moment capacity and flexural stiffness is 1.0-7.0% and 1.0-3.0%, respectively. As a result, to simplify the design calculation, the section parameters of a RAC-filled cold-formed steel RHS beam can be obtained by a RAC-filled welded steel RHS beam having the same geometry factors, and the tube yield strength of the latter is equal to that of the flat zone of the former.

Similar to the approach for the conventional CFST beams [17], calculation coefficient of moment capacity ( $\gamma_m$ ) of RAC-filled steel RHS beams is defined as follows:

$$\gamma_m = \frac{M_{u,fe}}{f_{scy,r} \cdot W_{scm}} \quad (4)$$

where,  $M_{u,fe}$  is the simulated moment capacity using the FE model,  $W_{scm}$  is the modulus of section, and  $f_{scy,r}$  is the strength factor of RAC-filled steel RHS and equals to  $f_{ck,r} \cdot (0.85\xi_r + 1.18)$  [9].

The influence of critical parameters on  $\gamma_m$  is depicted in Fig. 22, and the range of parameters is the same as those in Section 3.3. It is shown that,  $\gamma_m$  rises with the increase of  $r$ ,  $\alpha$  and  $f_y$  and the decrease of  $f'_c$ , and in general,  $\beta$  and sum of  $D$  and  $B$  have a relatively small effect. In addition, the variation of  $\gamma_m$  with  $r$ ,  $\alpha$ ,  $f_y$  and  $f'_c$  can be integrated into that with  $\xi_r$ , as indicated in Fig. 23. It can be observed that,  $\gamma_m$  generally increases with the augment of  $\xi_r$ . Through regression analysis of the simulated data in Fig. 23, a simplified calculation formula for  $\gamma_m$  can be reached:

$$\gamma_m = 0.48 \ln(\xi_r + 0.1) + 1.04 \quad (5)$$

The results in Fig. 23 demonstrate that Eq. (5) is a good predictor for  $\gamma_m$ , and the calculation results generally tend to be safe.

Therefore, the simplified equation for the moment capacity ( $M_u$ ) can be obtained by substituting Eq. (5) into Eq. (4):

$$M_u = [0.48 \ln(\xi_r + 0.1) + 1.04] \cdot f_{scy,r} \cdot W_{scm} \quad (6)$$

The simplified moment capacity ( $M_{u,s}$ ) is compared with the corresponding measured one ( $M_{u,e}$ )

of RAC-filled steel RHS beams with  $r$  of 0-100%, and a total of 133 data are collected. The variation of  $M_{u,s}/M_{u,e}$  with  $\beta$  and  $r$  is shown in Fig. 24. The statistical analysis of the data shows that, the mean and SD of  $M_{u,s}/M_{u,e}$  equal to 0.896 and 0.095, respectively, indicating that Eq. (6) can generally predict the moment capacity of RAC-filled steel RHS beams well. The applicable parameter conditions of the Eq. (6) are:  $(D+B) \leq 1600$  mm,  $r = 0 \sim 100\%$ ,  $\beta = 1.0 \sim 2.0$ ,  $\alpha = 0.05 \sim 0.2$ ,  $f_y = 235 \sim 420$  MPa, and  $f'_c = 25 \sim 75$  MPa.

Currently, the flexural stiffness of conventional CFST can be obtained by the method in the design codes. In this study, the design formulae in ACI 318 [32], ANSI/AISC 360 [37] and EN 1994-1-1 [38] were selected to predict the flexural stiffness ( $K$ ) of RAC-filled steel RHS, and the detailed equations are as follows:

$$K = \begin{cases} E_s \cdot I_s + 0.2E_c \cdot I_c & \text{ACI 318} \\ 0.64(E_s \cdot I_s + C_3 \cdot E_c \cdot I_c) & \text{ANSI/AISC 360} \\ E_s \cdot I_s + 0.6E_c \cdot I_c & \text{EN 1994-1-1} \end{cases} \quad (7)$$

where, the factor  $C_3$  is equal to  $0.45 + 3(A_s/A_g)$  and not greater than 0.9, in which  $A_s$  and  $A_g$  are cross-sectional area of steel RHS and gross area of composite section.

The comparison between the predicted ( $K_c$ ) and measured ( $K_e$ ) flexural stiffness is presented in Table 5, and a total of 71 valid experimental data with  $D$  and  $B$  of 100–254 mm and 60–254 mm respectively are included. It is shown that, the prediction of ANSI/AISC 360 is conservative with  $K_c$  about 22% lower than  $K_e$ ; however, EN 1994-1-1 is an unsafe predictor as  $K_c$  is on average 15.8% higher than  $K_e$ . Overall, ACI 318, which gives a mean of 0.902 and a SD of 0.156 respectively, is the best guidance for the flexural stiffness of RAC-filled steel RHS.

## 5. Conclusions

The static behaviour of recycled aggregate concrete (RAC)-filled steel rectangular hollow section (RHS) beams was comprehensively studied, and within the parameters investigated in the experiments and numerical simulations in this paper the following conclusions can be drawn:

(1) While subjected to flexural loading, RAC-filled steel RHS beams have good load-bearing capacity and deformability. When mid-span deflection larger than 6% of effective span, the failure

1 pattern of the specimens within the pure bending zone includes 2~4 local buckling on top flange and  
2 part of side walls of the tube, as well as crushing and cracking of concrete core at tube buckling sites  
3 and below the neutral axis, respectively. Moreover, the bottom flange of the tube of a few specimens  
4 also cracks in different degrees.  
5  
6

7  
8 (2) Generally, the relationship between moment ( $M$ ) and deformation in the mid-span section  
9 (deflection  $\delta_m$  and strain  $\varepsilon$ ) of the specimens goes through three stages of elastic, elastic-plastic and  
10 hardening sequentially. The deflections along effective span of the specimens basically accord with  
11 the sinusoidal half-wave, which becomes the basis for determining the mid-span section curvature.  
12 Simultaneously, for the mid-span section, the strain distribution along the depth generally accords  
13 with the assumption of 'plane sections remain plane after deformation', and the neutral axis, which  
14 has the feature of first rising and then falling, can continue to go up when reaching  $M_{u,e}$ .  
15  
16  
17  
18  
19  
20  
21  
22  
23  
24

25 (3) While keeping other parameters the same, the RAC-filled steel RHS beam specimens with a  
26 larger  $\beta$  and a smaller  $B/t$  have a higher  $M_{u,e}$  and  $K_e$ . Overall,  $M_{u,e}$  of the specimens with  
27  $\beta=1.5$  and  $2.0$  and  $B/t=31.1$  are 81.1~184.8% and 123.4% higher than those of the specimens with  
28  $\beta=1.0$  and  $B/t=60.9$ , and for  $K_e$  the percentage improvement equal to 167.1-475.2% and  
29 17.6~43.3%, respectively. In addition, the difference in  $M_{u,e}$  of the specimens with different  $r$  is  
30 within 5%; however,  $K_e$  of the specimens with  $r = 0$  is 2.5-15.9% higher than those of the  
31 specimens with  $r$  of 50% and 100%.  
32  
33  
34  
35  
36  
37  
38  
39  
40  
41  
42

43 (4) The comparison between simulation and experimental observations confirms that, the  
44 developed FE model is generally appropriate for simulating the static performance of RAC-filled  
45 steel RHS beams. The longitudinal stress ( $S_{33}$ ) of concrete core in the mid-span section while  
46 reaching the moment capacity reduces with the augment of  $\beta$  and  $r$ . Moreover, the interaction stress  
47 ( $p$ ) in compression zone is generally greater than that in tension zone, and  $p$  increases with the  
48 reduce of  $\beta$  and the increment of  $r$ .  
49  
50  
51  
52  
53  
54  
55  
56

57 (5) The moment capacity and the flexural stiffness of RAC-filled steel RHS beams can be  
58 accurately predicted by the simplified equations suggested in this study as well as the method in ACI  
59  
60  
61  
62  
63  
64  
65

318 code, respectively.

## Declaration of Competing Interest

The authors declare that they have no known competing financial interests or personal relationships that could have appeared to influence the work reported in this paper.

## Acknowledgements

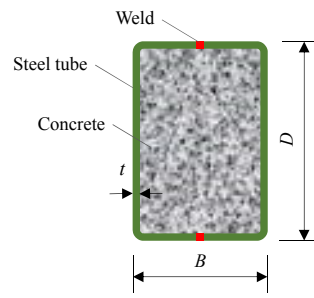
The research work reported herein was made possible by the National Natural Science Foundation of China (No. 51678105). The financial support is highly appreciated. The authors also wish to thank Ms. Xin-Na Xu for her help in the experiment.

## References:

- [1] B. Wang, L. Yan, Q. Fu, B. Kasal, A comprehensive review on recycled aggregate and recycled aggregate concrete, *Resour. Conserv. Recycl.* 171 (2021) 105565.
- [2] J. Nobre, M. Bravo, J. de Brito, G. Duarte, Durability performance of dry-mix shotcrete produced with coarse recycled concrete aggregates, *J. Build. Eng.* 29 (2020) 101135.
- [3] E. Vázquez, *Progress of Recycling in the Built Environment*, Final Report of the RILEM Technical Committee 217-PRE, Springer, Heidelberg, Germany, 2013.
- [4] J. Xiao, C. Wang, T. Ding, A. Akbarnezhad, A recycled aggregate concrete high-rise building: structural performance and embodied carbon footprint, *J. Clean Prod.* 199 (2018) 868–881.
- [5] Y.F. Yang, Modelling of recycled aggregate concrete-filled steel tube (RACFST) beam-columns subjected to cyclic loading, *Steel Compos. Struct.* 18 (1) (2015) 213–233.
- [6] Y.F. Yang, C. Hou, Behaviour and design calculations of recycled aggregate concrete filled steel tube (RACFST) members, *Mag. Concr. Res.* 67 (11) (2015) 611–620.
- [7] W. Li, J. Xiao, C. Shi, C.S. Poon, Structural behaviour of composite members with recycled aggregate concrete-an overview, *Adv. Struct. Eng.* 18 (6) (2015) 919–938.
- [8] L.H. Han, W. Li, R. Bjorhovde, Developments and advanced applications of concrete-filled steel tubular (CFST) structures: members, *J. Constr. Steel Res.* 100 (2014) 211–228.
- [9] Y.F. Yang, C. Hou, M. Liu, Tests and numerical simulation of rectangular RACFST stub columns under concentric compression, *Structures* 27 (2020) 396–410.
- [10] Y.F. Yang, F. Fu, X.M. Bie, Behaviour of rectangular RACFST slender columns under eccentric compression, *J. Build. Eng.* 38 (2021) 102236.

- 1  
2  
3  
4  
5  
6  
7  
8  
9  
10  
11  
12  
13  
14  
15  
16  
17  
18  
19  
20  
21  
22  
23  
24  
25  
26  
27  
28  
29  
30  
31  
32  
33  
34  
35  
36  
37  
38  
39  
40  
41  
42  
43  
44  
45  
46  
47  
48  
49  
50  
51  
52  
53  
54  
55  
56  
57  
58  
59  
60  
61  
62  
63  
64  
65
- [11] Y. Du, Z. Chen, J.Y.R. Liew, M.X. Xiong, Rectangular concrete-filled steel tubular beam-columns using high-strength steel: experiments and design, *J. Constr. Steel Res.* 131 (2017) 1–18.
- [12] M. Tomii, K. Sakino, Experimental studies on the ultimate moment of concrete filled square steel tubular beam-columns, *Trans. Archit. Inst. Japan* 275 (1979) 55–63.
- [13] Y.Q. Lu, D.J.L. Kennedy, Flexural behaviour of concrete-filled hollow structural sections, *Can. J. Civ. Eng.* 21 (1) (1994) 111–130.
- [14] B. Uy, Strength of concrete filled steel box columns incorporating local buckling, *J. Struct. Eng.* 126 (3) (2000) 341–352.
- [15] B. Uy, Strength of short concrete filled high strength steel box columns, *J. Constr. Steel Res.* 57 (2) (2001) 113–134.
- [16] W.M. Ghossein, D. Liu, Flexural behavior of high-strength rectangular concrete-filled steel hollow sections, *J. Constr. Steel Res.* 60 (11) (2004) 1681–1696.
- [17] L.H. Han, Flexural behaviour of concrete-filled steel tubes, *J. Constr. Steel Res.* 60 (2) (2004) 313–337.
- [18] L.H. Han, H. Lu, G.H. Yao, F.Y. Liao, Further study on the flexural behaviour of concrete-filled steel tubes, *J. Constr. Steel Res.* 62 (6) (2006) 554–565.
- [19] Y.F. Yang, L.H. Han, Compressive and flexural behavior of recycled aggregate concrete filled steel tubes (RACFST) under short-term loadings, *Steel Compos. Struct.* 6 (3) (2006) 257–284.
- [20] A. Jiang, J. Chen, W. Jin, Experimental investigation and design of thin-walled concrete-filled steel tubes subject to bending, *Thin-Walled Struct.* 63 (2013) 44–50.
- [21] Y.F. Yang, G.L. Ma, Experimental behaviour of recycled aggregate concrete filled stainless steel tube stub columns and beams, *Thin-Walled Struct.* 66 (2013) 62–75.
- [22] W.H. Wang, L.H. Han, W. Li, Y.H. Jia, Behavior of concrete-filled steel tubular stub columns and beams using dune sand as part of fine aggregate, *Construct. Build. Mater.* 51 (2014) 352–363.
- [23] Y. Chen, R. Feng, L. Wang, Flexural behavior of concrete-filled stainless steel SHS and RHS tubes, *Eng. Struct.* 134 (2017) 159–171.
- [24] M.F. Hassanein, O.F. Kharoob, M.H. Taman, Experimental investigation of cementitious material-filled square thin-walled steel beams, *Thin-Walled Struct.* 114 (2017) 134–143.
- [25] G. Li, D. Liu, Z. Yang, C. Zhang, Flexural behavior of high strength concrete filled high strength square steel tube, *J. Constr. Steel Res.* 128 (2017) 732–744.
- [26] M.X. Xiong, D.X. Xiong, J.Y.R. Liew, Flexural performance of concrete filled tubes with high tensile steel and ultra-high strength concrete, *J. Constr. Steel Res.* 132 (2017) 191–202.

- 1  
2  
3  
4  
5  
6  
7  
8  
9  
10  
11  
12  
13  
14  
15  
16  
17  
18  
19  
20  
21  
22  
23  
24  
25  
26  
27  
28  
29  
30  
31  
32  
33  
34  
35  
36  
37  
38  
39  
40  
41  
42  
43  
44  
45  
46  
47  
48  
49  
50  
51  
52  
53  
54  
55  
56  
57  
58  
59  
60  
61  
62  
63  
64  
65
- [27] Y.F. Yang, L. Zhang, X. Dai, Performance of recycled aggregate concrete-filled square steel tubular columns exposed to fire, *Adv. Struct. Eng.* 20 (9) (2017) 1340–1356.
- [28] Simulia, ABAQUS 6.14 Analysis User's Manual, Dassault Systemes Simulia Corp., Providence, RI, USA, 2014.
- [29] N. Abdel-Rahman, K.S. Sivakumaran, Material properties models for analysis of cold-formed steel members, *J. Struct. Eng.* 123 (9) (1997) 1135–1143.
- [30] M. Elchalakani, X.L. Zhao, R. Grzebieta, Tests on concrete filled double-skin (CHS outer and SHS inner) composite short columns under axial compression, *Thin-Walled Struct.* 40 (5) (2002) 415–441.
- [31] AISI, North American Specification for the Design of Cold-formed Steel Structural Members, American Iron and Steel Institute (AISI), North American Standard, Washington DC, USA, 2001.
- [32] ACI Committee 318, ACI 318-19-Building Code Requirements for Structural Concrete and Commentary, American Concrete Institute (ACI), Farmington Hills, Michigan, USA, 2019.
- [33] FIB, Fib Model Code for Concrete Structures 2010, Fédération Internationale du Béton, Ernst & Sohn, Berlin, Germany, 2013.
- [34] X. Xiang, C.S. Cai, R. Zhao, H. Peng, Numerical analysis of recycled aggregate concrete-filled steel tube stub columns, *Adv. Struct. Eng.* 19 (5) (2016) 717–729.
- [35] Z. Tao, Z.B. Wang, Q. Yu, Finite element modelling of concrete-filled steel stub columns under axial compression, *J. Constr. Steel Res.* 89 (2013) 121–131.
- [36] Y.F. Yang, Behaviour of recycled aggregate concrete-filled steel tubular columns under long-term sustained loads, *Adv. Struct. Eng.* 14 (2) (2011) 189–206.
- [37] AISC, ANSI/AISC 360-16, Specification for Structural Steel Buildings, American Institute of Steel Construction (AISC), Chicago, USA, 2016.
- [38] CEN, EN 1994-1-1, Eurocode 4: Design of composite steel and concrete structures-Part 1-1: General rules and rules for buildings, European Committee for Standardization, Brussels, Belgium, 2004.

**Figures:**

**Fig. 1.** Cross-section of the specimens.

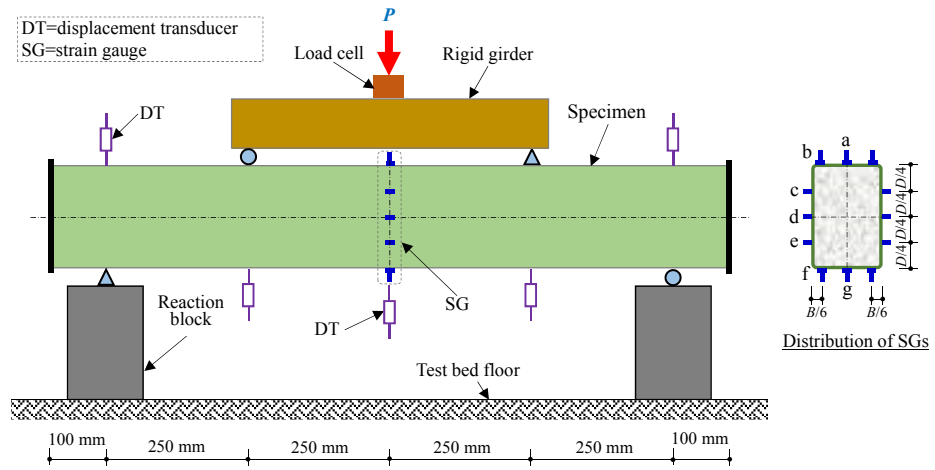
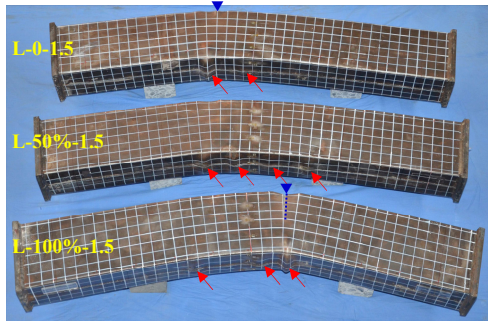
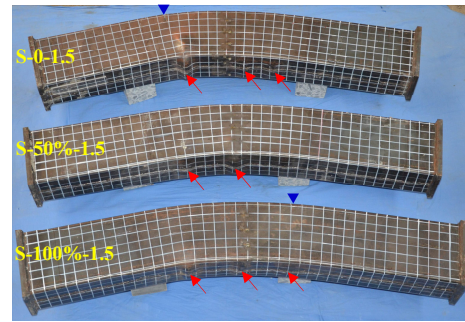


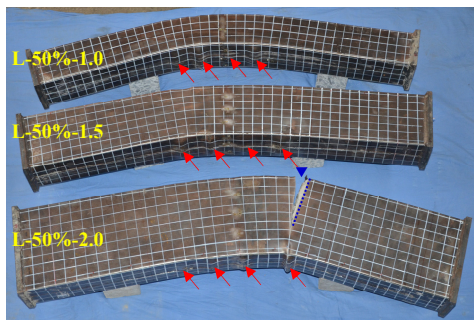
**Fig. 2.** Schematic diagram of test set-up and instrumentation.



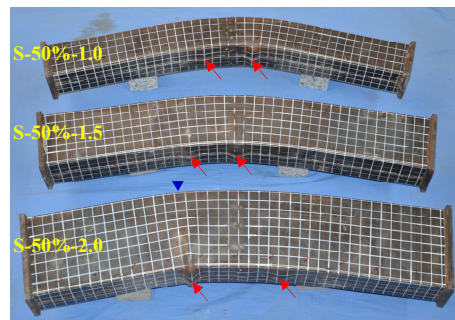
(a)  $B/t=60.9, \beta=1.5$



(b)  $B/t=31.1, \beta=1.5$

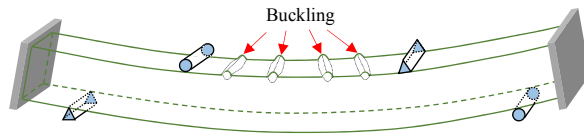


(c)  $B/t=60.9, r=50\%$

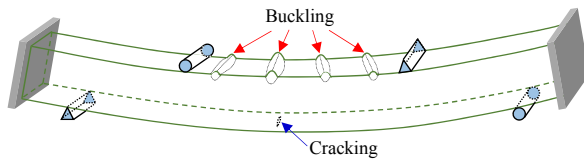


(d)  $B/t=31.1, r=50\%$

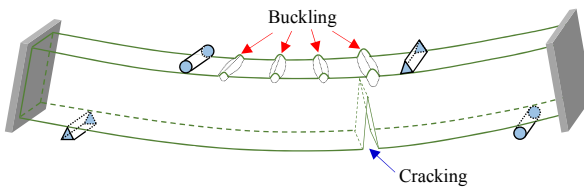
**Fig. 3.** Failure pattern of the specimens. (  $\blacktriangleright$  : local buckling;  $\blacktriangledown$  : cracking)



(a) Type I

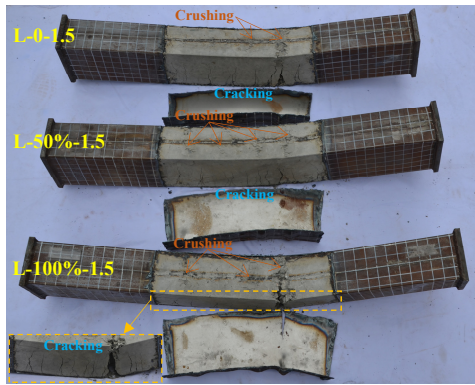


(b) Type II

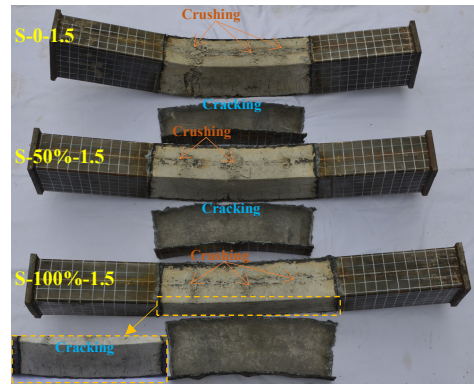


(c) Type III

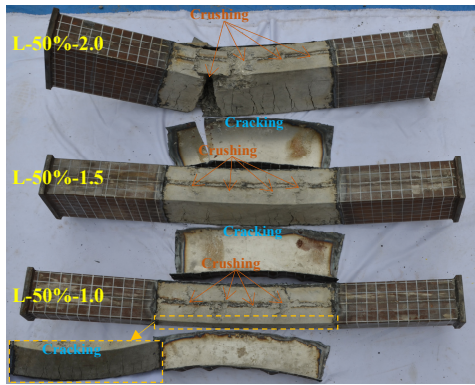
**Fig. 4.** Representative failure patterns of steel RHS.



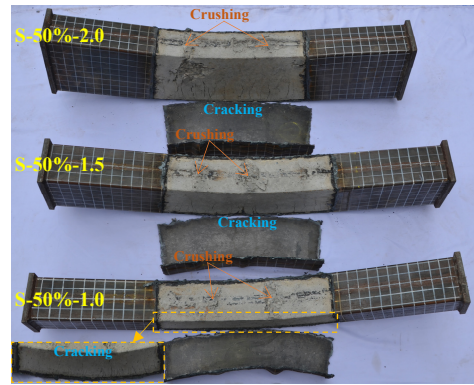
(a)  $B/t=60.9, \beta=1.5$



(b)  $B/t=31.1, \beta=1.5$

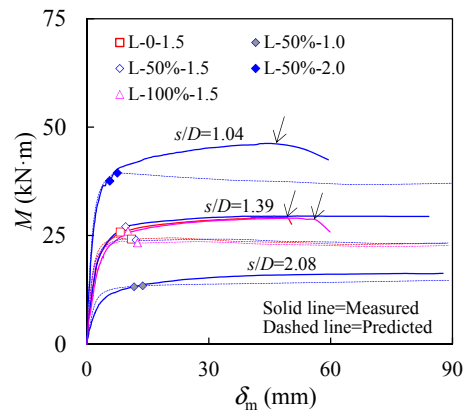


(c)  $B/t=60.9, r=50\%$

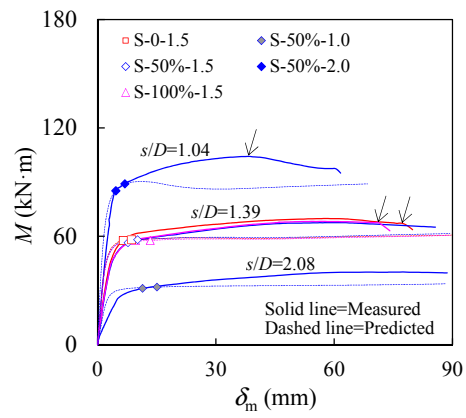


(d)  $B/t=31.1, r=50\%$

**Fig. 5.** Failure pattern of concrete core.

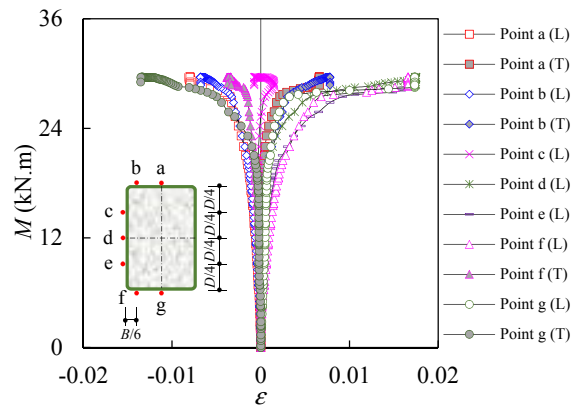


(a)  $B/t=60.9$

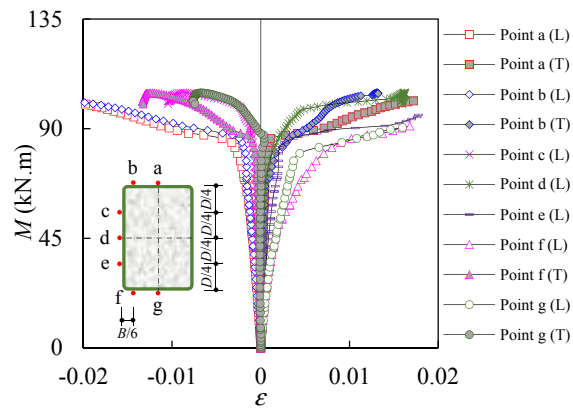


(b)  $B/t=31.1$

**Fig. 6.** Moment ( $M$ ) versus mid-span deflection ( $\delta_m$ ) curve of the specimens.

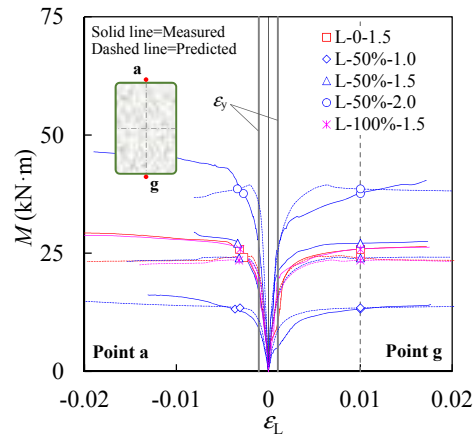


(a) L-50%-1.5

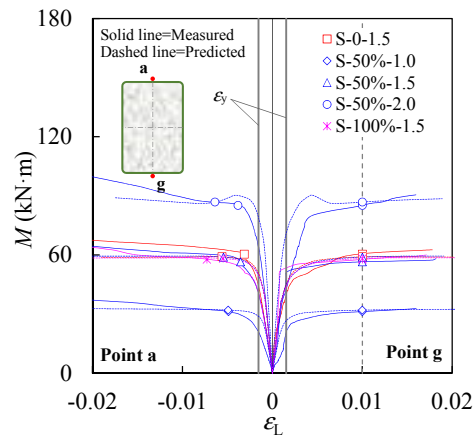


(b) S-50%-2.0

**Fig. 7.** Moment ( $M$ ) versus strain ( $\epsilon$ ) relationship of typical specimens.

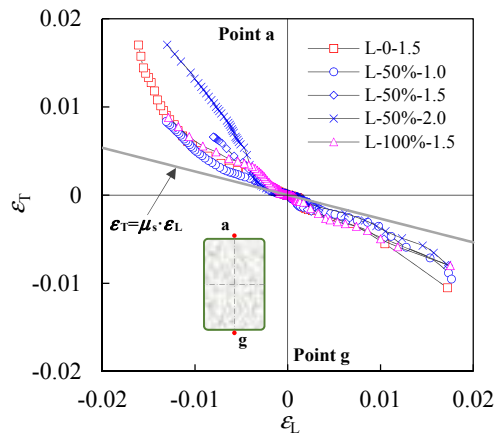


(a)  $B/t=60.9$

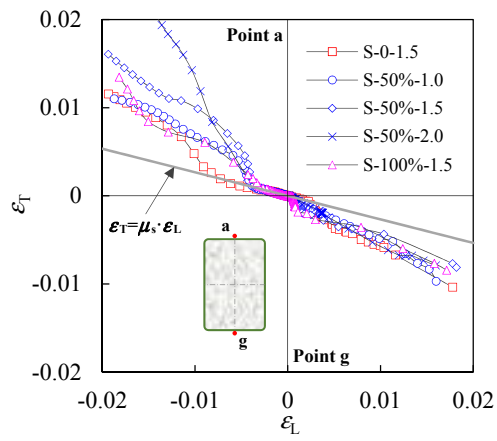


(b)  $B/t=31.1$

**Fig. 8.** Influence of parameters on  $M$ - $\epsilon_L$  relationship at points a and g.

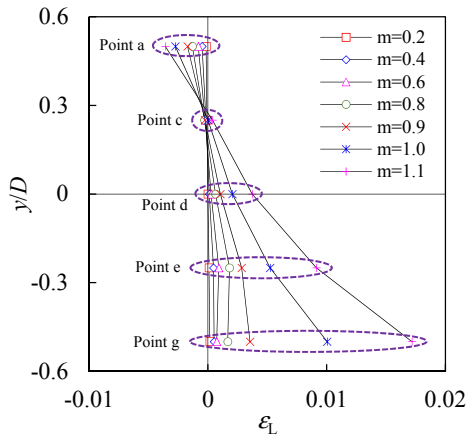


(a)  $B/t=60.9$

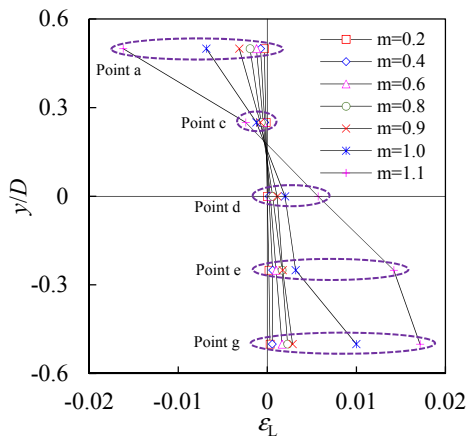


(b)  $B/t=31.1$

**Fig. 9.** Relationship between  $\epsilon_L$  and  $\epsilon_T$  at the midpoint of both flanges of the tube in the mid-span section.

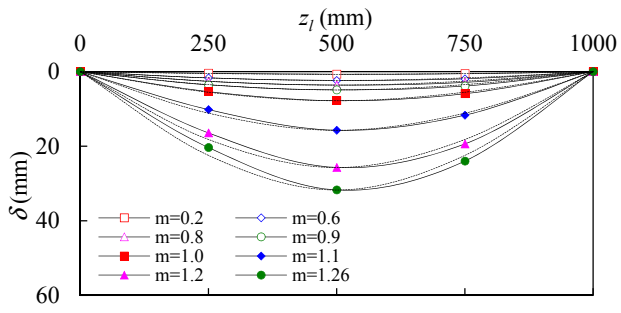


(a) L-50%-2.0

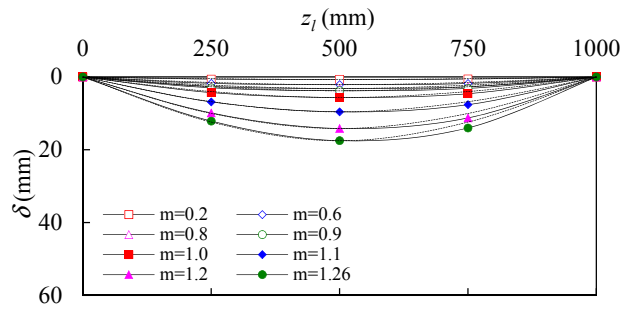


(b) S-100%-1.5

**Fig. 10.** Typical  $\epsilon_L$  distribution along the depth of the mid-span section.



(a) S-50%-1.5



(b) S-50%-2.0

**Fig. 11.** Deflections along the effective span of two typical specimens.

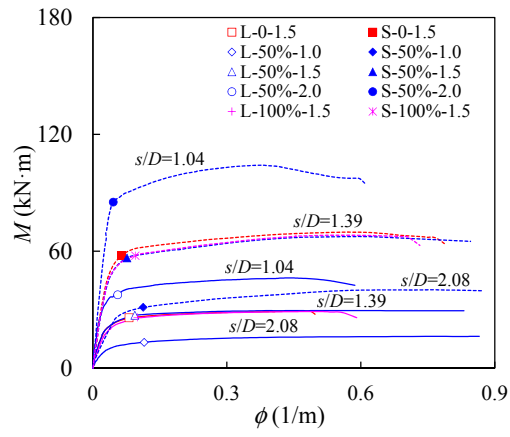
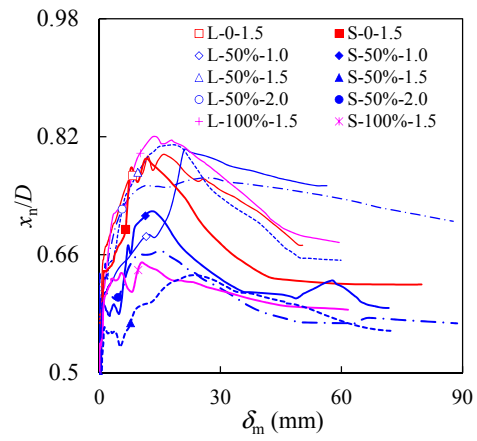
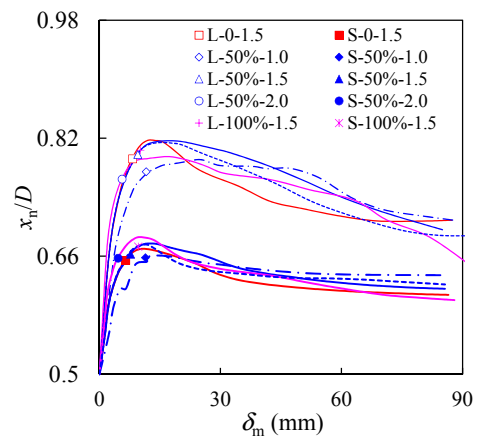


**Fig. 12.**  $M$ - $\phi$  relationship of the specimens.

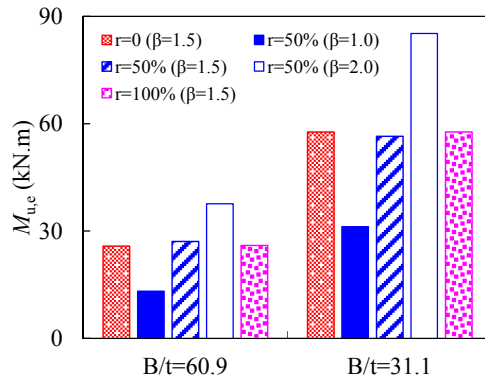


(a) Experimental

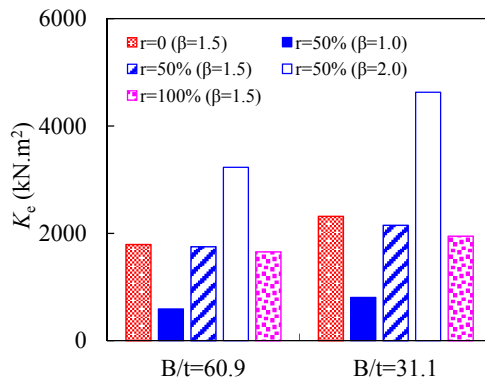


(b) Numerical

**Fig. 13.** Variation in relative position of neutral axis.



(a) Moment capacity



(b) Flexural stiffness

**Fig. 14.** Influence of experimental parameters on mechanical indexes.

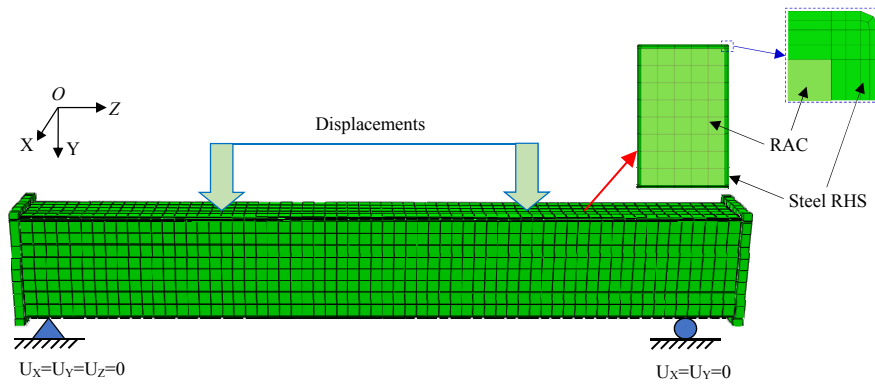
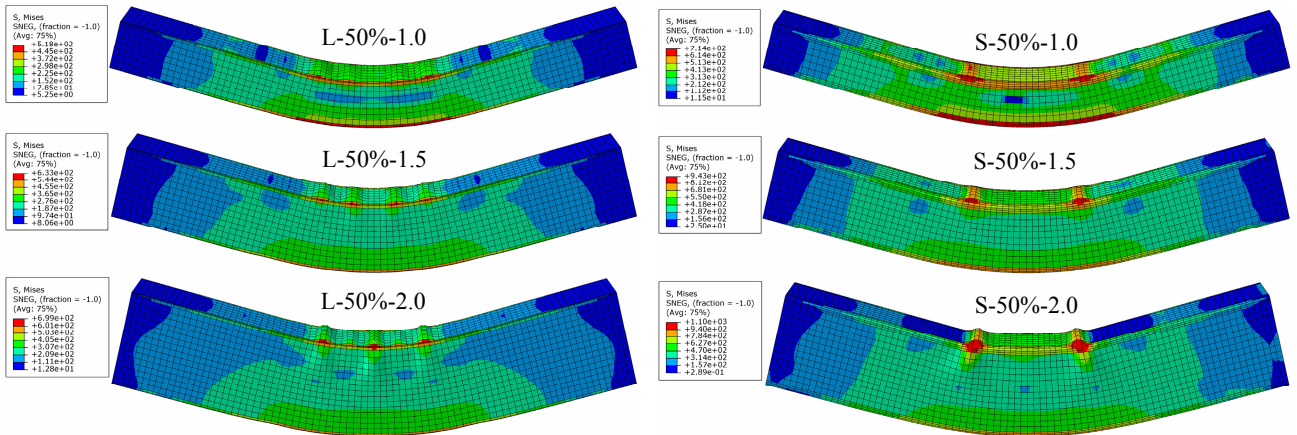
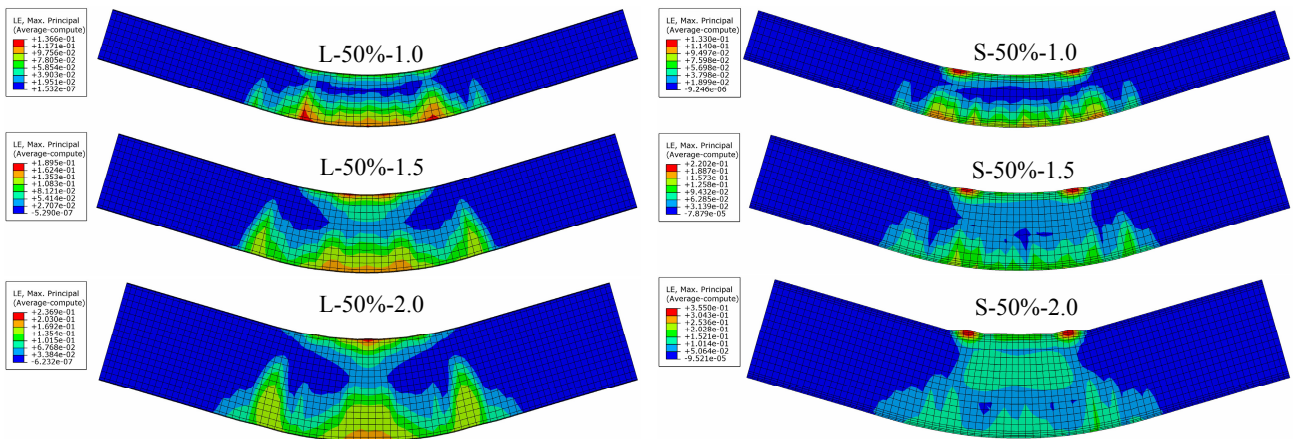


**Fig. 15.** Meshing and boundary conditions of the whole FE model.

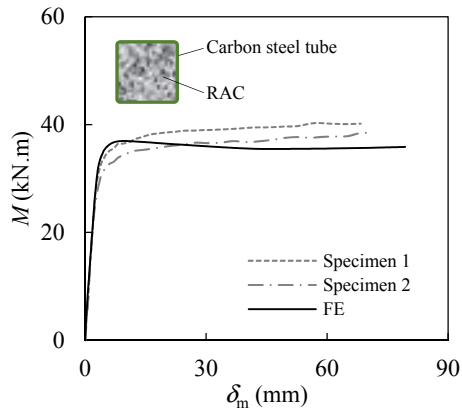


(a) Overall and outer tube

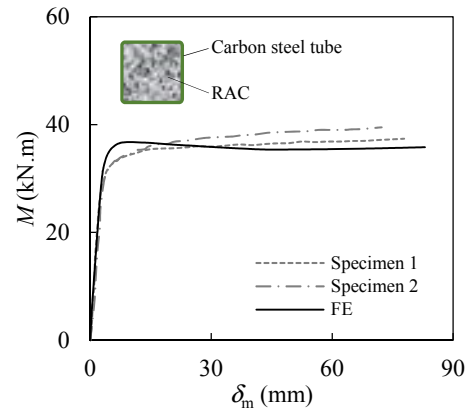


(b) Concrete core

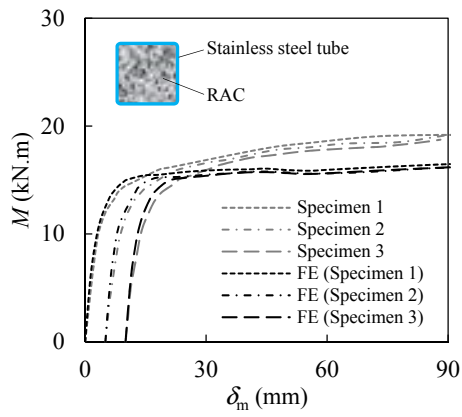
**Fig. 16.** The simulated failure patterns of typical specimens.



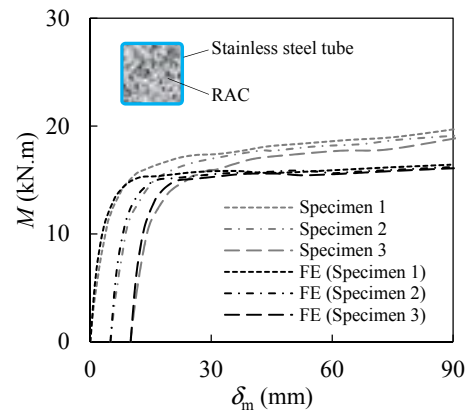
(a) BSb1 [19]



(b) BSb2 [19]



(c) S-B-C [21]



(d) S-B-F [21]

**Fig. 17.** Comparison between the simulated  $M$ - $\delta_m$  curves and the measured results in the literature.

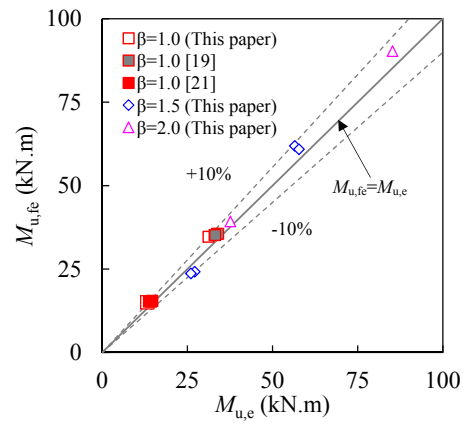
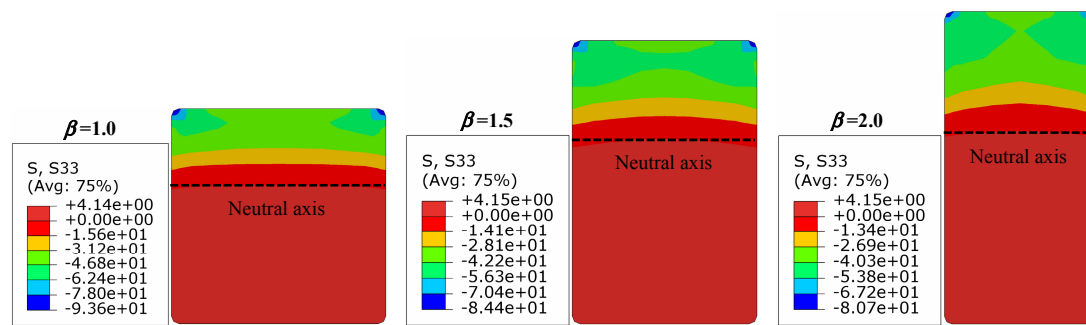
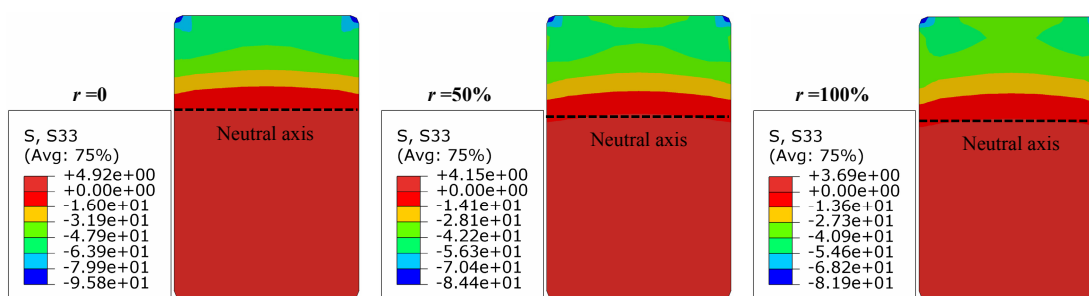


**Fig. 18.** Comparison between  $M_{u,fe}$  and  $M_{u,e}$  of RAC-filled steel RHS beams.

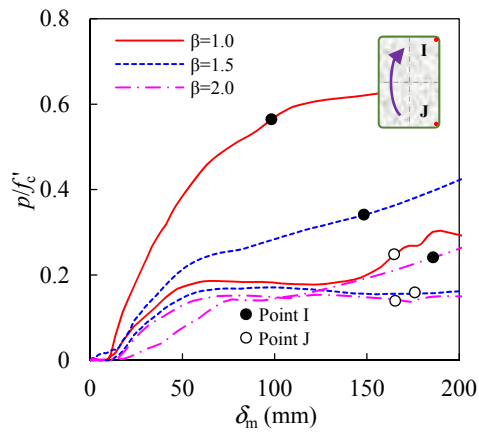


(a) Variation of  $\beta$

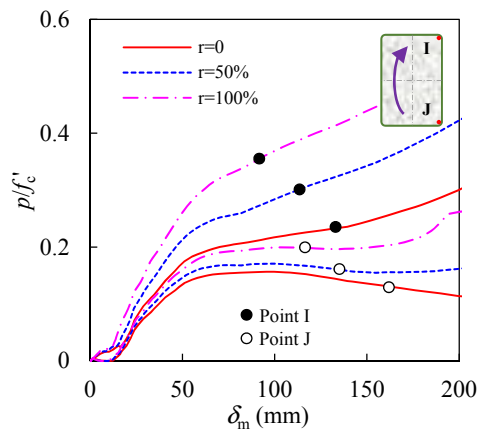


(b) Variation of  $r$

**Fig. 19.** Effect of  $\beta$  and  $r$  on longitudinal stress (S33) of concrete core.



(a) Variation of  $\beta$



(b) Variation of  $r$

**Fig. 20.** Influence of  $\beta$  and  $r$  on  $p/f'_c$  at specific positions.

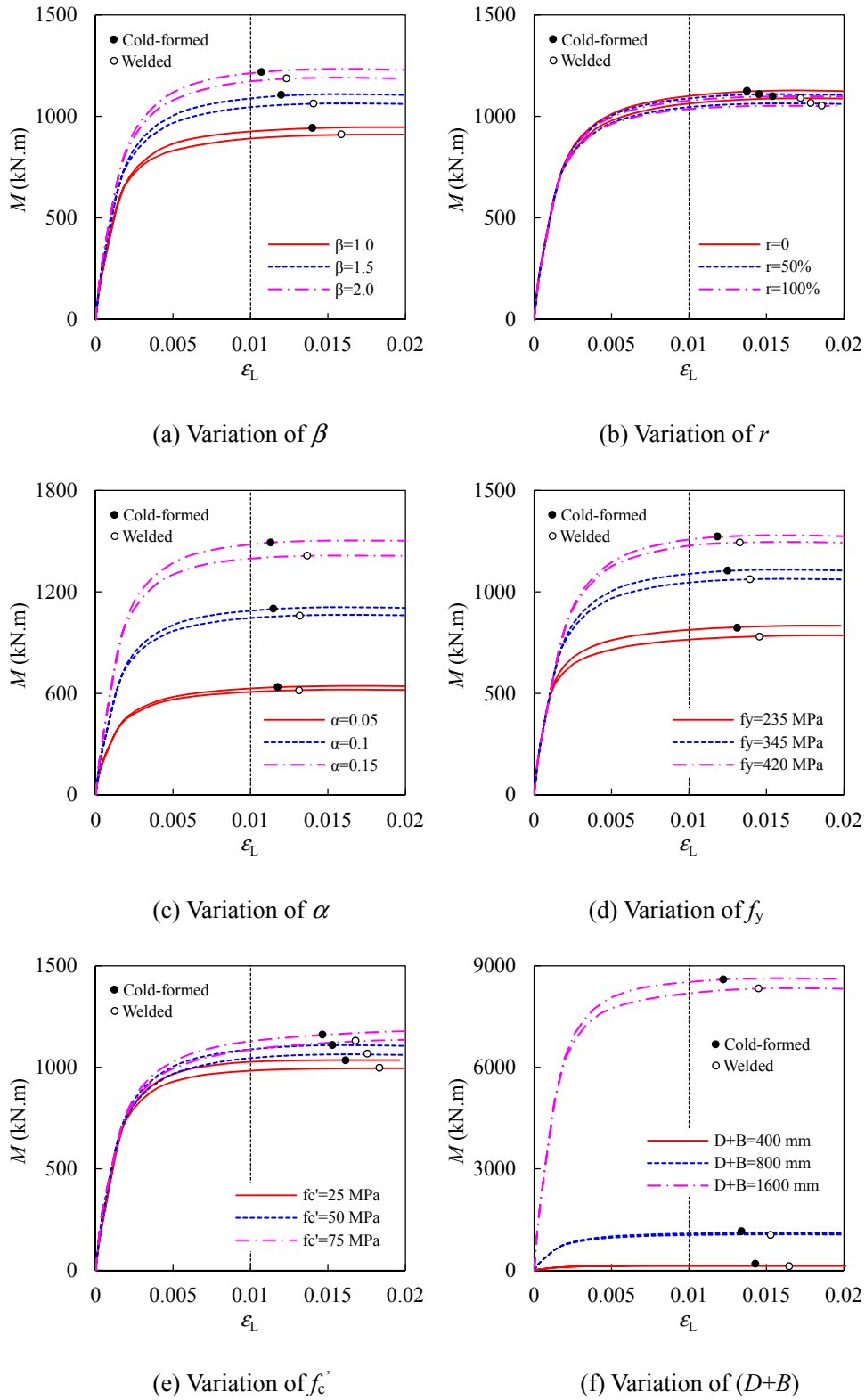
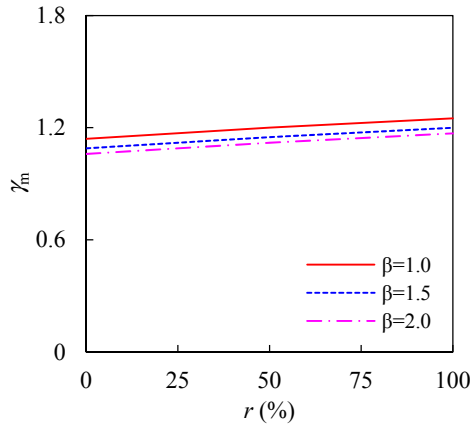
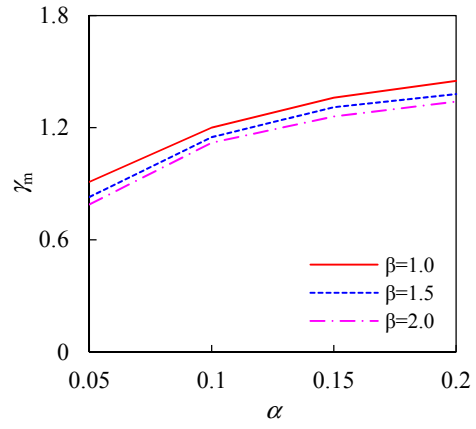


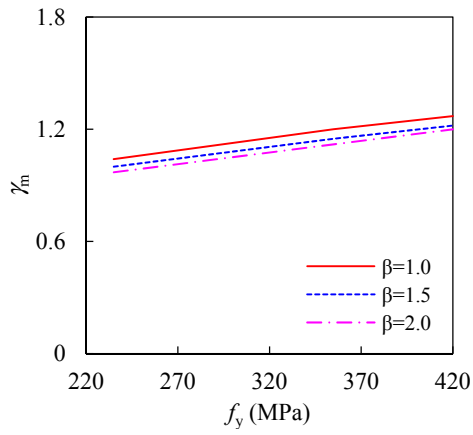
**Fig. 21.** Comparison of  $M-\epsilon_L$  curves of RAC-filled steel RHS beams with different outer tube.



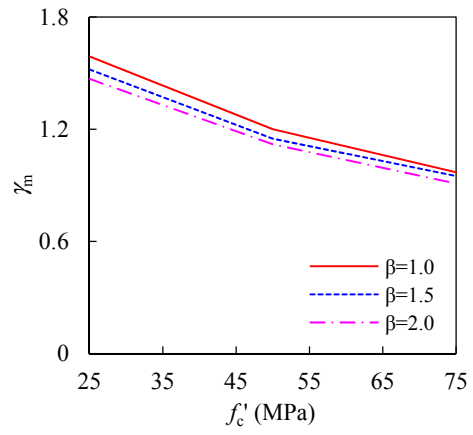
(a) Variation of  $r$  and  $\beta$



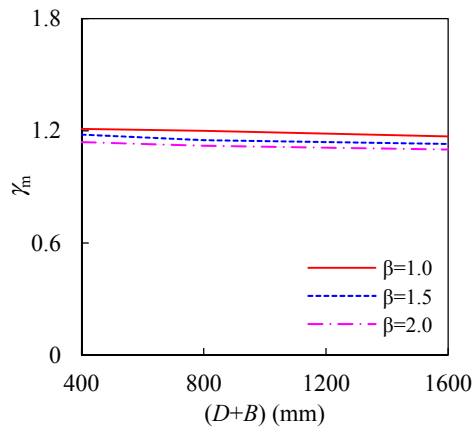
(b) Variation of  $\alpha$  and  $\beta$



(c) Variation of  $f_y$  and  $\beta$



(d) Variation of  $f'_c$  and  $\beta$



(e) Variation of  $(D+B)$  and  $\beta$

**Fig. 22.** Influence of critical parameters on  $\gamma_m$ .

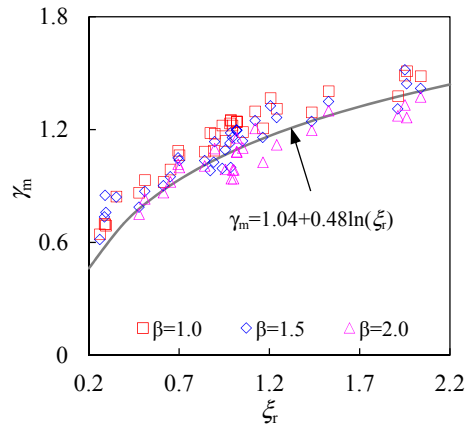


**Fig. 23.** Relationship between  $\gamma_m$  and  $\xi_r$ .

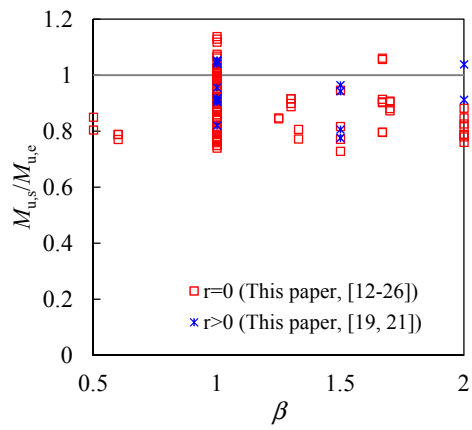


**Fig. 24.** Variation of  $M_{u,s}/M_{u,e}$  with  $\beta$  and  $r$ .

## Tables:

**Table 1** Summary of existing experiments on concrete-filled rectangular steel tube beams.

No.	$D$	$B$	$t$	$\beta$	$r$	Tube type*	Concrete Type <sup>+</sup>	NoS <sup>&amp;</sup>	Ref.
1	100	100	2.27-4.25	1.0	0	CS	NC	4	[12]
2	152, 254	152, 254	4.8-9.5	0.6-1.67	0	CS	NC	12	[13]
3	126-306	126-306	3.0	1.0	0	CS	NC	5	[14]
4	110-210	110-210	5.0	1.0	0	CS	NC	3	[15]
5	149.9-250.2	148.7-150.4	4.87-5.94	1.0-1.7	0	CS	NC	12	[16]
6	120, 150	60-120	2.93-5.86	1.0-2.0	0	CS	NC	16	[17]
7	100-200	100-200	3.0	1.0	0	CS	NC	18	[18]
8	150	150	2.94	1.0	0-50%	CS	NC+RAC	5	[19]
9	100.2-150.1	149.7-200.2	2.0, 3.0	0.5-1.0	0	CS	NC	4	[20]
10	120	120	1.77	1.0	0-75%	SS	NC+RAC	7	[21]
11	160-320	160	3.46	1.0-2.0	0	CS	DSC	6	[22]
12	60-100	50-100	1.1, 1.5	1.0, 2.0	0	SS	NC	16	[23]
13	99.5, 101.7	99.5, 101.7	1.82, 1.85	1.0	0	CS	CM	6	[24]
14	150	150	4.0-6.0	1.0	0	CS	NC	6	[25]
15	200	200	12, 12.5	1.0	0	CS	NC	3	[26]

1) \*: CS=carbon steel, and SS=stainless steel; 2) <sup>+</sup>: CM=cementitious materials, and DSC=concrete with dune sand; and 3) <sup>&</sup>: NoS=Number of specimens.

**Table 2.** Details of the specimens.

No.	Label	$D \times B \times t$ (mm×mm×mm)	$B/t$	$\beta$	$s/D$	$r$ (%)	$f_y$ (MPa)	$f_{cu}$ (MPa)	$M_{u,e}$ (kN·m)	$K_e$ (kN·m <sup>2</sup> )
1	L-0-1.5	180×120×1.97	60.9	1.5	1.39	0	195.8	61.8	25.8	1794.0
2	L-50%-1.0	120×120×1.97	60.9	1	2.08	50	195.8	61.0	13.2	591.3
3	L-50%-1.5	180×120×1.97	60.9	1.5	1.39	50	195.8	61.0	27.1	1750.0
4	L-50%-2.0	240×120×1.97	60.9	2	1.04	50	195.8	61.0	37.6	3230.4
5	L-100%-1.5	180×120×1.97	60.9	1.5	1.39	100	195.8	60.2	26.0	1656.9
6	S-0-1.5	180×120×3.86	31.1	1.5	1.39	0	325.3	61.8	57.7	2317.2
7	S-50%-1.0	120×120×3.86	31.1	1	2.08	50	325.3	61.0	31.2	805.7
8	S-50%-1.5	180×120×3.86	31.1	1.5	1.39	50	325.3	61.0	56.5	2152.3
9	S-50%-2.0	240×120×3.86	31.1	2	1.04	50	325.3	61.0	85.2	4629.5
10	S-100%-1.5	180×120×3.86	31.1	1.5	1.39	100	325.3	60.2	57.7	1948.9

**Table 3.** Properties of steel.

$t$ (mm)	$f_y$ (MPa)	$f_u$ (MPa)	$E_s$ (GPa)	$\varepsilon_y$ ( $\mu\varepsilon$ )	$\mu_s$	$e_f$ (%)
1.97	195.8	332.0	189.3	1034	0.268	49.7
3.86	325.3	499.6	203.1	1536	0.267	32.3